Medial-Guided Fuzzy Segmentation

George Stetten [1], Stephen Pizer [2]

[1] Department of Bioengineering, University of Pittsburgh,
Robotics Institute, Carnegie Mellon University.
[2] Medical Imaging Display and Analysis Group (MIDAG),
University of North Carolina, Chapel Hill.

Abstract. Segmentation is generally regarded as partitioning space at the boundary of an object so as to represent the object's shape, pose, size, and topology. Some images, however, contain so much noise that distinct boundaries are not forthcoming even after the object has been identified. We have used statistical methods based on medial features in Real Time 3D echocardiography to locate the left ventricular axis, even though the precise boundaries of the ventricle are simply not visible in the data. We then produce a fuzzy labeling of ventricular voxels to represent the shape of the ventricle without any explicit boundary. The fuzzy segmentation permits calculation of total ventricular volume as well as determination of local boundary equivalencies, both of which are validated against manual tracings on 155 left ventricles. The method uses a medial-based compartmentalization of the object that is generalizable to any shape.

1 Introduction

Real Time 3D (RT3D) ultrasound is an imaging modality developed in the early 1990's that electronically interrogates a volume in 3D using a matrix array of transducers instead of a conventional linear array [1]. Unlike 3D ultrasound techniques that rely on physically moving a linear array, the scan rate of RT3D ultrasound is rapid enough (22 frames/second) to smoothly sample heart wall motion of the left ventricle (LV) during a single cardiac cycle. The trade-off for operating at such a high speed in 3D is that the data is very noisy and the resolution is relatively poor, even for ultrasound.

Methods of finding and measuring the LV with conventional ultrasound have concentrated on deformable contours [2-6]. Deformable surfaces have been applied to mechanically scanned 3D echocardiographic data [7]. Attempts at applying deformable methods to Real Time 3D (RT3D) ultrasound, with its lower data quality, have not produced encouraging results [8]. The difficulties encountered when applying deformable models to RT3D ultrasound data have led us to review *bottom-up* approaches based on the measurement of geometric image properties. Successes have been reported in conventional ultrasound using circular arc matched filters to find cross sections of the ventricle [9]. Using templates to find the center of the ventricle and then fuzzy reasoning to find the boundary has also worked quite well [10]. In RT3D data, a Hough transform approach has been developed using circular edge filters, yielding fully automated measurement of balloons [11, 12]. All of these

S.L. Delp, A.M. DiGioia, and B. Jaramaz (Eds.): MICCAI 2000, LNCS 1935, pp. 226-235, 2000.

approaches possess fundamentally medial aspects, relating multiple boundary points to common central points deep within the object.

The lineage of the medial approach may be traced to the *medial axis* (otherwise known as the *symmetric axis* or *skeleton*) introduced on binary images by Blum and developed by Nagel, Nackman, and others [13-15]. Pizer has extended the medial axis to gray-scale images producing a graded measure called *medialness*, which links the aperture of the boundary measurement to the radius of the medial axis, to produce what has been labeled a *core*. A core is defined as a height ridge of medialness, a locus in a space of position, radius, and associated orientations [16-17]. Methods involving these continuous loci of medial primitives have proven robust against noise and variation in target shape [18]. We developed a particular method of finding medial loci that analyzes populations of medial primitives called *core atoms*, and uses *medial node models* to identify structures from sets of cores found in this manner. We successfully applied this method to finding the LV in RT3D data by means of a 3-node medial node model (Fig. 1A) demonstrating the automated location of the Apex-to-Mitral-Valve (AMV) axis (Fig. 1B) on 155 ventricles in RT3D ultrasound scans, as described elsewhere [19,20]. We describe here a continuation of that experiment in which a fuzzy segmentation method is applied to the LV, given the initial automated placement of the AMV axis and establishment of its global width. We validate the fuzzy segmentation method using the same 155 ventricles as before.

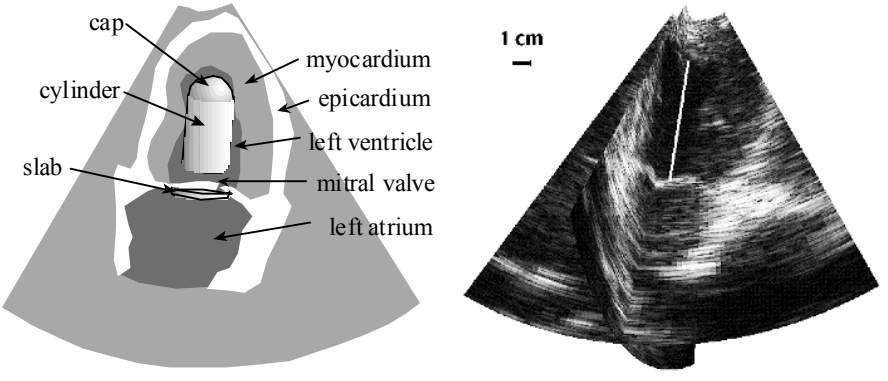

Fig. 1 **A.** Medial node model for left ventricle. **B.** Apex-to-mitral-valve (AMV) axis

2 Establishing the Probability of a Voxel Being in the LV

Given the extremely noisy data in the RT3D images of the heart, we have adopted a statistical approach to segmenting the LV. We assign a probability to individual voxels of being in the LV, as a function of both voxel intensity and location relative to the AMV axis. Dark voxels near the axis are likely to be in the LV. Voxels that are brighter and/or further from the axis are less likely to be in the LV. These two probabilites are combined into a single aggregate probability of being in the ventricle.

The probability $p_L(j)$ that voxel j is within the ventricle due to its location is determined by using a surface model of expected ventricular shape (Fig. 2). The midpoint of the AMV axis is the origin for a spherical coordinate system with the poles of the sphere being the end points of the AMV axis. The angle φ corresponds to *latitude*, with $\varphi = 0^\circ$ at the mitral valve and $\varphi = 180^\circ$ at the ventricular apex. The angle ω corresponds to *longitude*, or rotation around the AMV axis, with $0^\circ < \omega < 360^\circ$. The third coordinate r is the radial distance to the midpoint of the AMV axis.

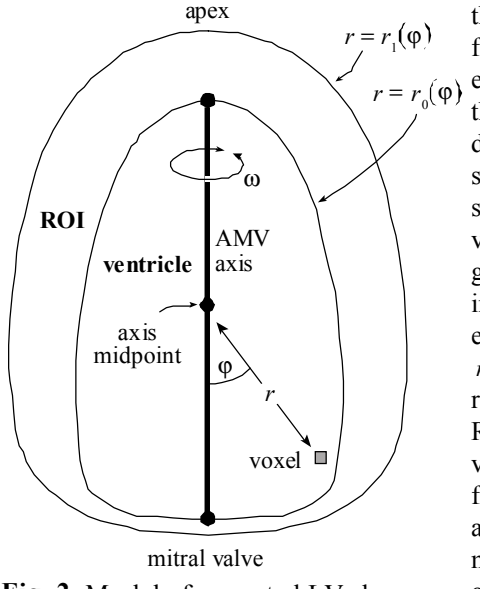

Fig. 2 Model of expected LV shape.

An expected surface for the ventricle is determined by a function $r_0(\varphi)$, such that $r = r_0(\varphi)$ at the LV surface. The function $r_0(\varphi)$ is constant to ω, exhibiting cylindrical symmetry around the AMV axis. A second surface, defining a region of interest (ROI), is specified by the function $r_1(\varphi)$. The ROI surrounds and includes the expected ventricular shape and will be used to generate regional statistics of voxel intensity. For the purposes of this experiment, the functions $r_0(\varphi)$ and $r_1(\varphi)$ have simply been drawn by hand to resemble a ventricle and a reasonable ROI surrounding and including the ventricle. Actual values have been taken from the drawing in Fig. 2, by measuring angles and distances from the axis midpoint. The model is scaled to fit the general size of each particular ventricle, as measured by the core atoms when they establish the AMV axis.

Given voxel j with angle φ and radius r, the probability $p_L(j)$ of it being in the ventricle is determined as a function of r using the probability function shown in Fig. 3A where $r_o(\varphi)$ is the expected distance to the ventricular boundary at latitude φ. Inside the boundary $r = r_0$, the probability is greater than $1/2$, whereas outside it is less than $1/2$.

Ventricular voxels are darker than surrounding voxels, although overall intensity in ultrasound images varies unpredictably from one scan to another. To compensate for this, the probability $p_I(j)$ of voxel j being within the ventricle, given only its intensity, is based on a statistical study of voxels in the ROI for a particular scan. The mean intensity $\bar{I}$ of all voxels in the ROI is computed, weighting each voxel's intensity $I(j)$ by its $p_L(j)$:

$$\bar{I} = \frac{\sum_{j \in ROI} p_L(j) I(j)}{\sum_{j \in ROI} p_L(j)} . \quad (1)$$

Thus ventricular voxels are favored by their tendency to be located near the AMV axis, although other voxels are represented as well. The value of $\bar{I}$ reflects the particular intensities of voxels in the image and is used in the function shown in Fig. 3B to compute the probability $p_I(j)$ for each voxel, given its intensity. The functions in Fig. 3A and Fig 3B have been drawn *ad hoc* for the purposes of this experiment. Determining corresponding functions to optimize the accuracy of the resulting segmentation is beyond the scope of the present research.

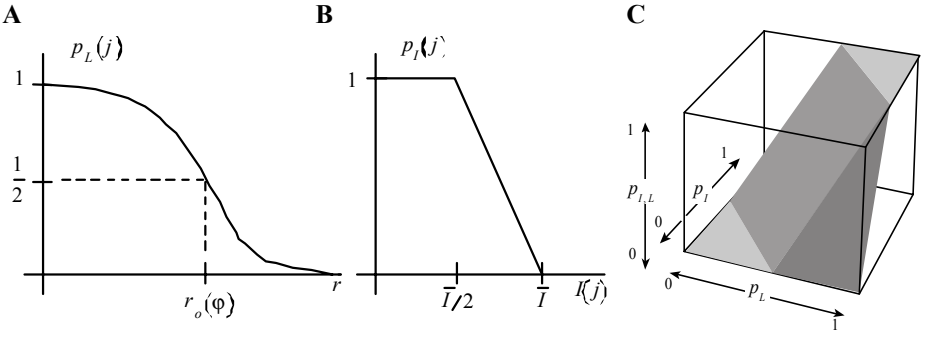

Fig 3 Probabilities $p_L(j)$, $p_I(j)$, and their aggregate probability $p_{I,L}(j)$.

For fuzzy segmentation, we need a single probability $p_{I,L}(j)$ that voxel j is in the ventricle, given both its intensity and location. We define an operator A such that $P_{I,L}(j) = A(P_I(j), P_L(j))$, and design it to exhibit the following behaviors:

(1) It is monotonic with positive slope for both $p_I(j)$ and $p_L(j)$, mapping the domain $[0,1]$ for $p_I(j)$ and $p_L(j)$ into a range $[0,1]$ for $p_{I,L}(j)$.
(2) If either argument $p_I(j)$ and $p_L(j)$ is equal to $1/2$, then $p_{I,L}(j)$ equals the other argument, so that a probability of $1/2$ exerts neither positive nor negative influence.
(3) If either $p_I(j)$ or $p_L(j)$ is 0, then $p_A(j)$ is also 0, so that either can independently exclude any voxel from the ventricle.

A continuous, piece-wise linear function that satisfies the above constraints is shown in Fig. 3C. The aggregate probability $p_{I,L}(j)$ represents a fuzzy segmentation of the LV, as will be validated in the following section.

3 Validating the Fuzzy Segmentation Method

We validated the method for fuzzy segmentation by computing volumes and local boundary equivalencies using $p_{I,L}(j)$ and comparing these results to manual tracings. (A more detailed record of these results and other aspects of this research is available in the author's dissertation [19].) The same 155 ultrasound scans used to establish the AMV axis in the previous experiment [20] were divided blindly into training and test sets. The training set was used to optimize the method's parameters in terms of accuracy of volume measurement and to measure bias using linear regression. Of the many parameters in the overall process, those that were adjusted included the shapes of the surface model in Fig. 2 and the probability curves in Figs. 3A and 3B. The method was then applied to the test set without further adjustment of parameters.

In Fig. 4A, an example of an ROI (bright) encompassing the LV surface model (dark) is shown located, oriented, and scaled by the AMV axis information. The probability $p_L(j)$ was computed for each voxel. An example of $p_L(j)$ for one image is shown in Fig. 4B. A weighted mean of voxel intensity $\bar{I}$ within the ROI was computed and $p_I(j)$ found for each voxel. The aggregate probability $p_{I,L}(j)$ was then computed. As may be seen in Fig. 5A, $p_{I,L}(j)$ is affected by both $p_L(j)$, which dominates the overall distribution, and $p_I(j)$, which accounts for finer detail, including the dark areas in the mitral valve and septal wall.

An automated ventricular volume was calculated by summing the product of $p_{I,L}(j)$ and its corresponding voxel volume over the ROI. Three sets of manual tracings were performed by a single operator on slices orthogonal to the AMV axis (Fig 5B). Voxels within the traces were labeled and used to compute a manual ventricular volume. A comparison between automated and manual volumes is shown in Fig. 6., with an RMS error of 25.9 ml. A reduced RMS error of 9.2 ml was achieved by measuring volume *change* with time for a given heart. This is clinically significant since volume change can yield stroke volume and short-term variation in heart function.

To localize error, the concept of *truncated wedges* was developed. A full description of truncated wedges may be found elsewhere [19]. The basic concept is to divide an arbitrary shape into compartments that extend from the surface to the medial manifold (Fig. 7). For the particular case of the sphere (Fig. 7a), voxels are sorted by φ and ω into bins and volumes computed for each wedge (solid angle). An equivalent radius is then computed for each wedge given its volume and compared to a radius determined from the manual tracings. The results are shown in Fig. 8.

The local error is expressed in terms of linear distance (cm) as a function of latitude φ and longitude ω. The S.D. for the 3 manual tracings is between 1.5-3.5 mm, while the automated segmentation produces an RMS error generally between 2-6 mm with a spike up to 1.6 cm (which we believe to be caused by the aorta leaving the LV -- a feature of the anatomy not included in the manual tracing).

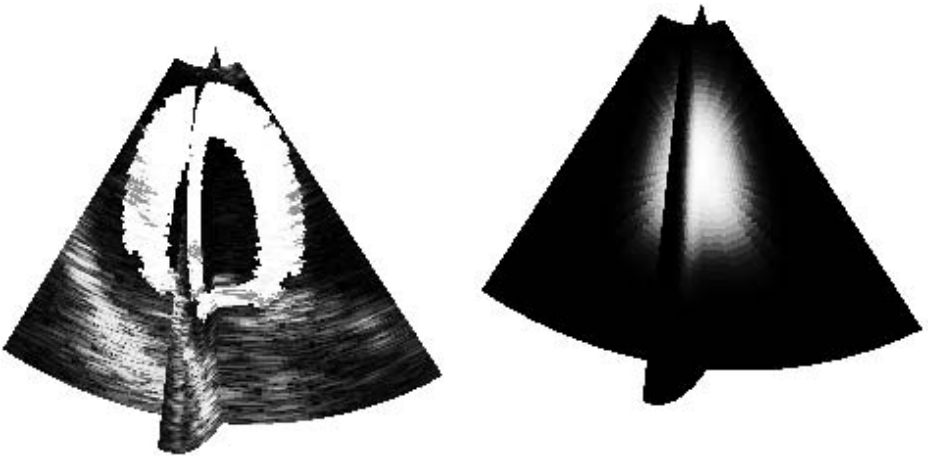

Fig. 4 **A.** ROI (bright) and LV surface model (dark). **B.** $p_L(j)$ for each voxel, bright = 1 and dark = 0

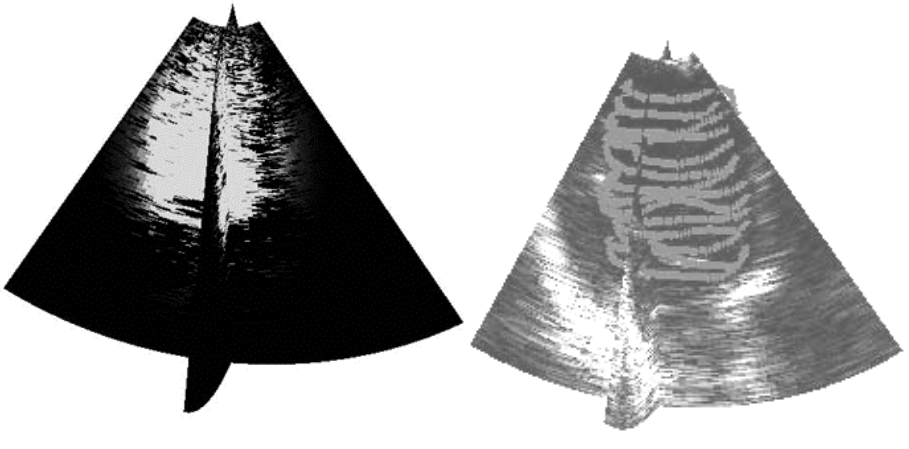

Fig. 5 **A.** Aggregate probability $p_{I,L}(j)$. **B.** Manual tracings of LV.

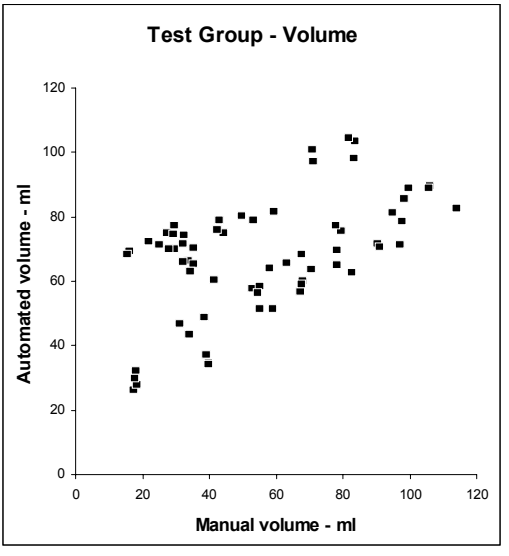

Fig. 6 Manual vs. automated volume.

The accuracy of any segmentation is not well judged solely by comparing total volumes, since an object's volume says nothing about its location and since different shapes may have the same volume. Using the medial framework already established, local error between the manual and automated segmentations was determined in spherical coordinates φ, ω, and r. Longitude ω was not a parameter in the ventricular surface model, but since all the scans were performed with the same transducer orientation, the error could be correlated as a function of both φ and ω.

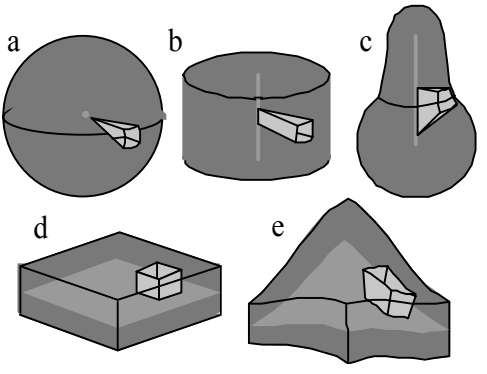

Fig. 7 Truncated wedges based on the medial manifold.

4 Conclusions

Most segmentation routines attempt to locate complete and precise boundaries, which provide explicit parameters for measurements. Perhaps such boundaries seem a more accurate portrayal of physical reality, because, after all, most real surfaces are defined at a microscopic scale and interact with light in a manner easily interpretable by human vision. A probabilistic representation of a surface may be just as useful and

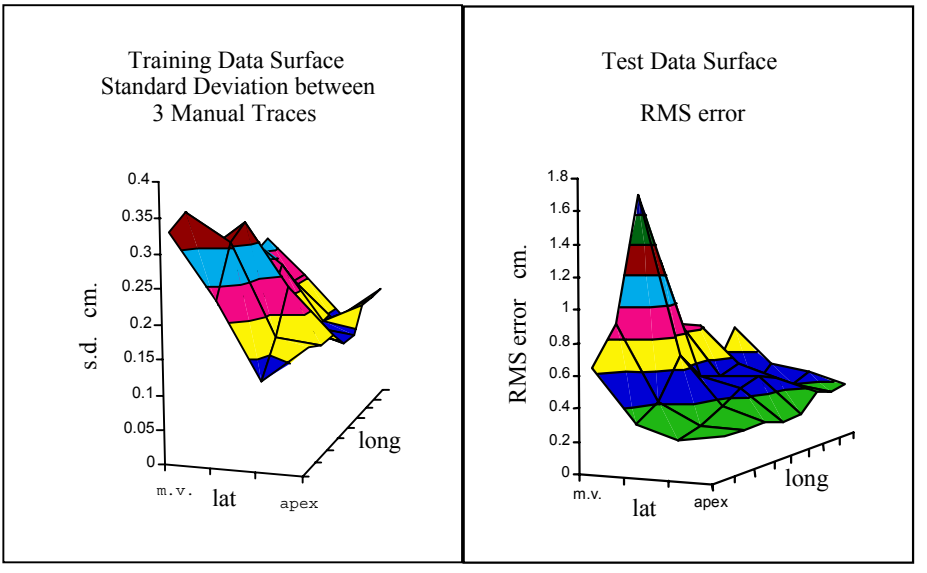

Fig. 8 **A.** S.D. between manual tracings. **B.** RMS error of automated segmentation.

more robust for making geometric measurements, but it is not easily visualized or understood. It is clear from Fig. 5A that our fuzzy segmentation method does not yield a reasonable probability for each individual voxel. The fuzzy representation lacks a distinct topology. Only in certain statistical operations, such as the computation of volume, is the fuzzy shape representation appropriate. In those cases, accuracy of measurements based on probabilistic boundaries can be assessed against those from manually determined boundaries.

We believe the inconclusive results from the RT3D ultrasound data may be as much a problem with the manual tracings as with the method itself, and we make no pretense to have optimized the numerous parameters in the method on such a small sample. We merely report an empirical test of a new concept. The use of a medial framework to calculate $p_L(j)$ within an aggregate probability, and to weight an intensity histogram relative to that framework, are promising new avenues of research. In concert with medial node models and truncated wedges, the fuzzy segmentation method can be applied to anatomical targets of any shape.

Support from a Whitaker Biomedical Engineering grant, NSF grant CDR8622201, NIH grants 1K08HL03220, P01CA47982, and HL46242, with data generously supplied by Takahiro Shiota, Department of Cardiology, Cleveland Clinic Foundation, and by Volumetrics Medical Imaging, Inc., Durham, NC.

References

1. Stetten, G., T. Ota, C. Ohazama, C. Fleishman, J. Castelucci, J. Oxaal, T. Ryan, J. Kisslo, and O.v. Ramm, *Real-Time 3D Ultrasound: A New Look at the Heart.* Journal of Cardiovascular Diagnosis and Procedures, 1998. **15**(2): p. 73-84.
2. Chalana, V., D.T. Linker, D.R. Haynor, and Y. Kim, *A multiple active contour model for cardiac boundary detection on echocardiographic sequence.* IEEE Transactions on Medical Image, 1996. **15**(3): p. 290-298.
3. Hozumi, T., K. Yoshida, H. Yoshioka, T. Yagi, T. Akasaka, T. Tagaki, M. Nishiura, M. Watanabe, and J. Yoshikawa, *Echocardiographic estimation of left ventricular cavity area with a newly developed automated contour tracking method.* Journal of the American Society of Echocardiography, 1997. **10**(8): p. 822-829.
4. Mikic, I., S. Krucinski, and J.D. Thomas, *Segmentation and tracking in echocardiographic sequences: Active contours guided by optical flow estimates.* IEEE Transactions on Medical Imaging, 1998. **17**(2): p. 274-284.
5. Malassiotis, S. and M.G. Strintzis, *Tracking the left ventricle in echocardiographic images by learning heart dynamics.* IEEE Transactions on Medical Imaging, 1999. **18**(3): p. 282-290.
6. Hunter, I.A., J.J. Soraghan, J. Christie, and T.S. Durrani. *Detection of Echocardiographic Left Ventricle Boundaries Using Neural Networks*. in *Computers in Cardiology*. 1993, London, UK, : p. 201-204
7. Coppini, G., R. Poli, and G. Valli, *Recovery of the 3-D shape of the left ventricle from echocardiographic images.* IEEE Transactions on Medical Imaging, 1995. **14**(2): p. 301-317.
8. Stetten, G., T. Irvine, D. Ritscher, O.T.v. Ramm, J. Panza, V. Sachdev, J. Castellucci, M. Jones, and D. Sahn. *Improved accuracy for a semi-automated method for computing right ventricle (RV) cavity volumes from Real Time 3D Echo: Comparison studies to ultrasonic crystals in an open-chest animal model*. in *American College of Cardiology 48th Scientific Sessions*. 1999 (in press), New Orleans
9. Wilson, D.C., E.A. Geiser, and J. Li, *Feature extraction in two-dimensional short-axis echocardiographic images.* Journal of Mathematical Imaging and Vision, 1993. **3**: p. 285-298.
10. Feng, J., W.C. Lin, and C.T. Chen, *Epicardial Boundary Detection Using Fuzzy Reasoning.* IEEE Transactions on Medical Imaging, 1991. **10**(2): p. 187-199, .
11. Stetten, G. and R. Morris, *Shape detection with the Flow Integration Transform.* Information Sciences, 1995. **85**: p. 203-221.
12. Stetten, G., M. Caines, C. Ohazama, and O.T.v. Ramm, *The Volumetricardiogram (VCG): Volume Determination of Cardiac Chambers using 3D Matrix-Array Ultrasound.* Proceedings of the SPIE Symposium on Medical Imaging, 1995. **2432**: p. 185-196.
13. Blum, H. and R.N. Nagel, *Shape description using weighted symmetric axis features.* Pattern Recognition, 1978. **10**: p. 167-180.
14. Nackman, L.R., *Curvature relations in 3D symmetric axes.* CVGIP, 1982. **20**: p. 43-57.

15. Nackman, L.R. and S.M. Pizer, *Three-Dimensional shape description using the symmetric axis transform I:Theory.* IEEE Transactions on Pattern Analysis and Machine Intelligence, 1985. **2**(2): p. 187-202.
16. Burbeck, C.A. and S.M. Pizer, *Object representation by cores: Identifying and representing primitive spatial regions.* Vision Research, 1995. **35**(13): p. 1917-1930.
17. Pizer, S.M., D.H. Eberly, B.S. Morse, and D.S. Fritsch, *Zoom invariant vision of figural shape: the mathematics of cores.* Computer Vision and Image Understanding, 1998. **69**(1): p. 55-71.
18. Morse, B.S., S.M. Pizer, D.T. Puff, and C. Gu, *Zoom-Invariant vision of figural shape: Effect on cores of image disturbances.* Computer Vision and Image Understanding, 1998. **69**: p. 72-86.
19. Stetten, G., *Automated Identification and Measurement of Cardiac Anatomy Via Analysis of Medial Primitives*, Doctoral Dissertation in Dept. Biomedical Engineering, University of North Carolina, Chapel Hill, 1999, http://www.stetten.com/george/publications/phd
20. Stetten, G.D. and S.M. Pizer, *Medial Node Models to Identify and Measure Objects in Real-Time 3D Echocardiography.* IEEE Transactions on Medical Imaging, 1999. **18**(10): p. 1025-1034.